Lattice model for spontaneous imbibition in porous media: The role of effective tension and universality class

Deok-Sun Lee,[1] Zeinab Sadjadi,[2] and Heiko Rieger[2]

[1]*Department of Physics, Inha University, Incheon 402-751, Korea*
[2]*Theoretical Physics, Saarland University, 66041 Saarbrücken, Germany*

Recently, anomalous scaling properties of front broadening during spontaneous imbibition of water in Vycor glass, a nanoporous medium, were reported: the mean height and the width of the propagating front increase with time t both proportional to $t^{1/2}$. Here, we propose a simple lattice imbibition model and elucidate quantitatively how the correlation range of the hydrostatic pressure and the disorder strength of the pore radii affect the scaling properties of the imbibition front. We introduce an effective tension of liquid across neighboring pores, which depends on the aspect ratio of each pore, and show that it leads to a dynamical crossover: both the mean height and the roughness grow faster in the presence of tension in the intermediate-time regime but eventually saturate in the long-time regime. The universality class of the long-time behavior is discussed by examining the associated scaling exponents and their relation to directed percolation.

I. INTRODUCTION

Moving interfaces in disordered media occur in various physical situations and have been studied theoretically for some decades now [1,2]. It has been demonstrated that a few characteristics such as the embedding dimension, the conservation laws, and the kind of nonlinearity emerging in a coarse grained equation of motion determine the scaling behavior of the moving interfaces and establish a few universality classes regardless of the microscopic details [1–3].

Imbibition, the propagation of a fluid into the nonwetting region found in, e.g., oil recovery, printing, irrigation, filtration, etc. [4], is also characterized by the motion and morphology of the interface between the liquid and the nonwetting region. Contrary to other interfaces, the theoretical understanding of the imbibition front dynamics is far from complete, as it varies significantly between different experimental setups and between different models [4–6]. Moreover, the global conservation of the liquid volume generates nontrivial correlations in the hydrostatic pressure in the liquid, which affects the dynamics of the imbibition front. Pore-network models [7–11] and dynamical equations [12–15] have been proposed and analyzed to understand various features of imbibition.

Studies have found that the mechanisms underlying drainage and imbibition are related to the diffusion-limited aggregation [16] or the invasion percolation [17] depending on the ratio of viscous and capillary force and the pore geometry [6,7]. For spontaneous imbibition, when a wetting liquid is drawn into a porous medium by capillary forces without external force, it is well known that the balance between the viscous drag and the pressure gradient in the bulk leads to the Lucas-Washburn law [18,19] saying that the average height of the imbibition front increases proportionally to the square root of time. Far less clear is the roughening dynamics of the imbibition front, i.e., the time dependence of the height fluctuations: By focusing on the quenched disorder in the medium, the relations to the directed-percolation-depinning (DPD) model [20,21], the quenched Kardar-Parisi-Zhang universality (QKPZ), or the quenched Edwards-Wilkinson

(QEW) universality classes [22] have been suggested. But, recently it was emphasized that in addition to quenched disorder, nonlocal interactions due to the fluid-conservation law are crucial for the imbibition front roughening [11,23].

A novel universality class in the imbibition front broadening was recently identified during the spontaneous imbibition of water in nanoporous Vycor glass, a silica substrate of low porosity consisting of nanometer-sized elongated pores [11]: The mean height of the interface and its roughness are *both* found to increase with time t as $\sim t^{1/2}$. Since the ratio of the roughness to the mean height usually decreases with time during roughening dynamics, but is constant in this case, the interface roughening appears anomalously strong.

A pore-network model [11], in which liquid within the pores propagates according to Hagen-Poiseuille's law, was capable to reproduce the experimentally observed features of the imbibition front in Vycor glass. This suggested that the imbibition front consists of disconnected menisci and that the hydrostatic pressure in the bulk and the capillary pressure at these menisci are essential for understanding the experimentally observed anomalous roughening. An essential feature of the pore-network model proposed in Ref. [11] was the emergence of meniscus arrests at pore junctions with branches of unequal radii. A subsequent scaling theory for the meniscus arrest time distribution presented in Ref. [24] predicted, in accordance with results from computer simulations or the pore-network model, that arrest times of menisci in the thicker branches of pore junction indeed scales with the height of the junction where the arrest occurred. In this way, the proposed theory could explain the proportionality between height and roughness in random networks of elongated pores [24].

Nevertheless, the robustness of the observed scaling behavior is not yet understood. Given many other kinds of kinetic interfaces displaying scaling behavior different from those for imbibition, it is natural to ask what factors are responsible for these differences. To address this issue, we design in this paper a minimal lattice model of imbibition and explore how the structure and dynamics of the interface depend on the parameters. The proposed lattice imbibition model has similarities with other lattice growth models but involves

as a new feature the hydrostatic pressure, which generates long-range correlation. We adopt an approximation method of estimating the hydrostatic pressure, which captures the essence of the pressure profile generated by the liquid flow under the Hagen-Poiseuille's law and the volume conservation.

We find that the disorder in the pore radii and the long correlation length of the pressure, which will be explained in detail in the next sections, are essential for the observed scaling behavior of spontaneous imbibition. If the pore radii are uniform or the pressure correlation spans only a short scale, the roughness becomes very weak characterized by different scaling exponents from those observed in the experiment. It has been argued that the absence of an effective tension acting across adjacent pores underlies the anomalous scaling in the experiment. Computer simulations of our lattice imbibition model show that both the mean height and the roughness display a crossover in time and eventually saturate when the effective tension is present. In particular, they grow commonly as $t^{0.7}$ in the intermediate-time regime before saturation, which is a faster growth with time than without the tension. The formation of voids is suppressed due to the effective tension, making the cluster of filled pores appear compact. We discuss the intermediate-time behavior and the universality class in connection with the properties of the directed percolation (DP) cluster.

The paper is organized as follows. The lattice imbibition model is introduced in Sec. II. The impact of the strength of the pore radii and the lateral pressure correlation range are studied in Secs. III and IV. In Sec. V, we perform the finite-size scaling analysis of the mean height and the roughness as functions of time and present the associated scaling exponents. Our findings are summarized and discussed in Sec. VI.

II. MODEL

We consider a two-dimensional network of $\mathcal{N} = N \times L$ pores inclined at $45°$ as shown in Fig. 1(a). Each pore, indexed $n = 0, 1, 2, \dots, \mathcal{N} - 1$ from the bottom left to the top right, is cylindrical and has radius r_n selected randomly between $1 - \Delta$ and $1 + \Delta$ with $0 \leqslant \Delta < 1$. Here, Δ characterizes the strength of the disorder in the pore radii. The area of the intersections is supposed to be negligible, such that an intersection is immediately filled once one of its adjacent pores is filled [6,11]. The configurations with larger intersections compared to pores have been studied, e.g., in Ref. [8]. The Boolean variable f_n of pore n takes 1 or 0 if it is filled or empty, respectively. The pressure $p_{(x,y)}$ represents the hydrostatic pressure at (x, y). Initially, all the pores are empty, $f_n = 0$ for all n. The lower ends of the bottom pores ($0 \leqslant n \leqslant N - 1$) are immersed in the liquid such that the hydrostatic pressure at $y = 0$ is kept constant, here taken as zero, i.e., $p_{(x,0)} = 0$. The atmospheric pressure in the empty pores is also set to zero. Periodic boundary conditions are applied in the x direction.

The time evolution of the liquid configuration $\{f_n\}$ describes the liquid propagation through the pore network. The interface $\mathcal{I}$ between wet and dry regions is identified with the set of empty pores having at least one filled nearest-neighbor pore [see Fig. 1(a)]. In order to update the liquid configuration $\{f_n\}$, an empty pore s is chosen randomly among the interface pores. Then, one of its filled neighbors s' is selected. The
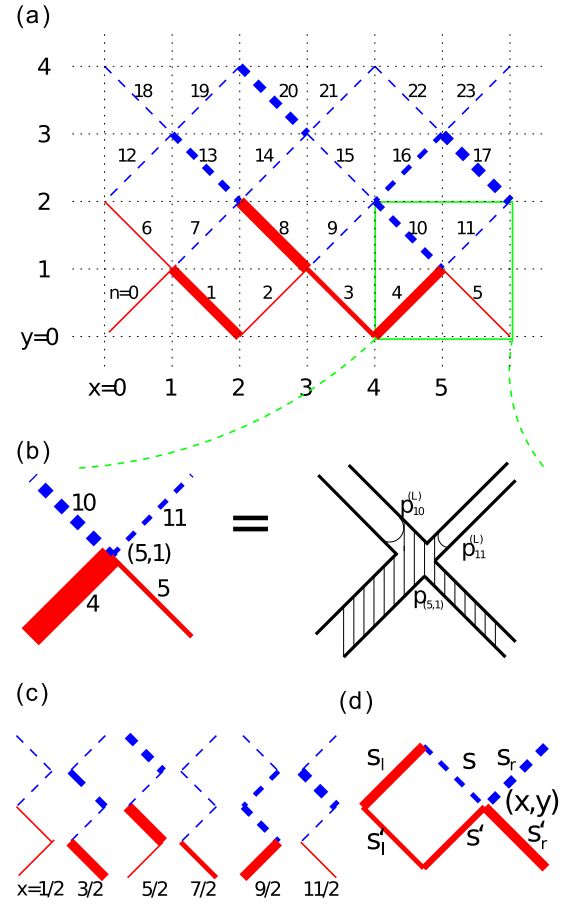

FIG. 1. (Color online) Lattice imbibition model. (a) Two-dimensional network of $\mathcal{N} = N \times L$ pores with $N = 6$ and $L = 4$. Pores are indexed $n = 0, 1, 2, \dots, \mathcal{N} - 1$ from the left bottom to the right top. Solid (red) and dashed (blue) lines indicate filled and empty pores, respectively. The coordinates $(\bar{x}_n, \bar{y}_n)$ of the center of a pore n are given by $\bar{x}_n = n - N \lfloor \frac{n}{N} \rfloor + \frac{1}{2}$ and $\bar{y}_n = \lfloor \frac{n}{N} \rfloor + \frac{1}{2}$ and with $\lfloor x \rfloor$ the integer not larger than x. The interface $\mathcal{I}$ consists of the pores $n = 7, 9, 10, 11, 12, 13, 14$. (b) $p_{10}^{(L)}$ is the Laplace pressure at the free end of the meniscus in pore $n = 10$ and $p_{(5,1)}$ is the hydrostatic pressure at $(5,1)$. (c) Six independent vertical columns from (a). For the column at $x = \frac{5}{2}$, the pore $n = 8$ is the highest filled pore, the upper end of which is at $y = 2$, and the pressure in the column is given by $p_{(5/2,y)}^{(0)} = (y/2) p_8^{(L)}$ for $0 \leqslant y < 2$ and 0 for $y \geqslant 2$ according to Eq. (3). (d) The effective tension $T_{s,s'} = I$ in case of $f_{s_\ell} = 1, f_{s_r} = 0$, and $f_{s'_r} = 1$.

driving force $P_{s,s'}$ acting on s from s' is computed. If $P_{s,s'}$ is positive, the pore s is filled with probability $\min\{P_{s,s'}, 1\}$. If $P_{s,s'}$ is negative, the pore s' is evacuated by the retraction of liquid with probability $\min\{|P_{s,s'}|, 1\}$. This procedure is repeated as many as the number of interface pores, and then the macroscopic time t is increased by 1.

The liquid propagates spontaneously upward (in the $+y$ direction) due to the capillary pressure [see Fig. 1(a)]. The pressure at the free end of the meniscus of pore s is the Laplace pressure

$$p_s^{(L)} = -\frac{2\sigma}{r_s}, \tag{1}$$

where r_s is the radius of pore s and σ is the surface tension set to $\sigma = \frac{1}{2}$. Note that here the surface tension σ is different from the effective tension acting across distinct pores considered in this work. Such low pressure at the menisci generates pressure gradient in the bulk and enables the liquid to propagate through the pores; $p_{(x,y)}$ decreases with y ($p_{(x,0)} = 0$). Let (x, y) be the junction of the selected interface pore s and its filled neighbor pore s'. If liquid were to fill the pore s, the difference between the hydrostatic pressure at the junction and the Laplace pressure at the meniscus,

$$\Delta p_{s,s'} = \max \left\{ p_{(x,y)} - p_s^{(L)}, 0 \right\}, \qquad (2)$$

contributes to the driving force $P_{s,s'}$ pushing the liquid to fill the interface pore s [see Fig. 1(b)]. If $p_{(x,y)}$ is lower than $p_s^{(L)}$, the pressure difference is taken to be zero as it does not contribute to the driving force [11]. Such piston-type displacement of meniscus is a main mechanism of imbibition [25]. The snap-off, filling pores by the collapse of wetting fluid creeping the pore wall, is another mechanism but can be neglected in our model system; snap-off happens when $p > p^{(S)} = -\sigma/r$ while the piston-type motion happens when $p > p^{(L)} = -2\sigma/r$ [6,25]. Given such small radii of pores as 4 nm in the experiment of [11], the impact of viscosity or gravity can be also neglected compared with the capillary force. The capillary number, the ratio of viscous to capillary force given by $Ca = \eta v / \sigma$ with η viscosity of water and v the velocity of the imbibition front, is ranging between 10^{-6} to 10^{-8} decreasing with time as the velocity is reduced. The Bond number is about 10^{-9}, which is the ratio of the gravity to the capillary force and defined as $B = (\rho_{\text{water}} - \rho_{\text{air}})gr^2/\sigma$ with ρ_{water} and ρ_{air} the density of water and air and g the gravitational acceleration. Detailed physical mechanisms of imbibition in various systems have been investigated by Lenormand, Blunt, and others, including the works by two of the authors [4,6–8,11,24,25].

The pressure $p_{(x,y)}$ is determined by the boundary conditions, liquid-volume conservation, and Hagen-Poiseuille's law of incompressible fluid. Under the boundary conditions at the bottom ($p_{(x,0)} = 0$) and the update rules described above, the pressure $p_{(x,y)}$ exhibits an important feature: it rarely varies with x but decreases linearly with y as illustrated in Fig. 2 for the pore-network model in Refs. [11,24].

Instead of calculating the pressure field $p_{(x,y)}$ as in Refs. [11,24] we use the following simplified model for $p_{(x,y)}$. Let us first consider the simple case that all the vertical columns of pores are separated as in Fig. 1(c) and the pore s is filled. In each column at $x' = \frac{1}{2}, \frac{3}{2}, \frac{5}{2}, \ldots, N - \frac{1}{2}$, the pressure $p_{(x',y)}^{(0)}$ decreases linearly from 0 to $p_{\hat{n}_{x'}}^{(L)}$, where $\hat{n}_{x'}$ is the index of the highest filled pore in that column:

$$p_{(x',y)}^{(0)} = \begin{cases} \frac{y}{\hat{y}_{x'}} p_{\hat{n}_{x'}}^{(L)} & \text{for } y < \hat{y}_{x'}, \\ 0 & \text{for } y \geqslant \hat{y}_{x'}, \end{cases} \qquad (3)$$

where $\hat{y}_{x'}$ is the y coordinate of the upper end of the filled highest pore, indexed by $\hat{n}_{x'}$, in the given column at x'. In Eq. (3), we assumed that the pores beneath the highest filled one are filled.

Since the columns at different lateral coordinates x' are connected, the pressure field $p_{(x,y)}$ will be laterally correlated due to fluid volume conservation. We therefore define the
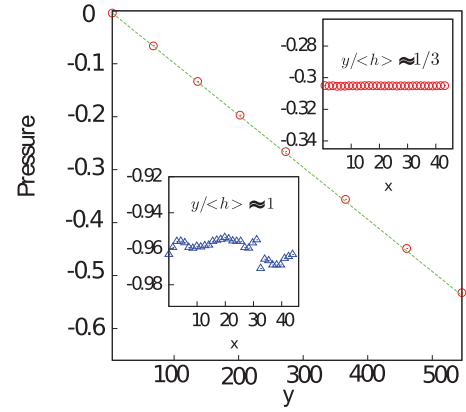

FIG. 2. (Color online) Variation of the hydrostatic pressure with height (y) obtained from the pore-network model [11,24]. The pressure linearly decreases with height y in a specific time. The dashed line is a linear fit to the data. Insets: Pressure variation in terms of x at two different fixed heights. The pressure does not vary considerably in the x direction.

true hydrostatic pressure field $p_{(x,y)}$ to be an average over neighboring values of $p_{(x',y)}^{(0)}$'s at the same height:

$$p_{(x,y)} = \frac{\sum_{|x-x'|<R} p_{(x',y)}^{(0)}}{\sum_{|x-x'|<R} 1}, \qquad (4)$$

where R is a model parameter showing the lateral correlation range of pressure. This approximation is motivated by the observation that the pressure rarely varies with x as shown in Fig. 2 and thus R is set to be infinite. We will set the parameter R free, however, to study theoretically the effect of its reduction from infinite to a finite value on the roughening process. Actually, the correlation range R can be changed by viscosity or depending on time and location, e.g., near the imbibition front that is irregular and rough as shown in Fig. 2.

Finally, let us define an effective tension as a force which reduces the energetic cost associated with the front width. In Refs. [6,7], it was shown that the imbibition front becomes compact and smooth as the capillary number increases, implying that the effective tension can be important depending on the capillary number [4]. The viscosity η and the surface tension σ of displacing and displaced fluids change the capillary number. More relevant to the experiments in Ref. [11], the aspect ratio $\ell/(2r)$ with ℓ the length and r the radius of a pore can change the capillary number and the effective tension. From the Hagen-Poiseuille's law in the pore-network model [11], it holds that the velocity of fluid inside a pore s is given by $v \sim r_s^2 p_s^{(L)}/(\ell_s \eta) \sim (r_s/\ell_s)(\sigma/\eta)$, which suggests that the capillary number $Ca = \eta v/\sigma$ is inversely proportional to the aspect ratio on the average. This relationship between the aspect ratio and the effective tension is understandable as follows. When the aspect ratio of each pore is small, the adjacent menisci unite and form a continuous interface, thus the interface roughening is mainly slowed down by the effective tension. On the other hand, if the aspect ratio is very large, this effective tension is negligible as there is no continuous interface. In our model, when the filled neighbor pore s' is right below the interface pore s, the effective tension

can affect the liquid propagation. In this case, the pore s is more likely to be filled if its left or right neighbor is already filled. On the contrary, if the left or right neighbor of the filled pore s' is empty, the pore s' may be evacuated to reduce the interface length. These impacts of the effective tension can be modeled by

$$T_{s,s'} = I \times \left[\max\left(f_{s_\ell}, f_{s'_\ell} - 1 \right) + \max\left(f_{s_r}, f_{s'_r} - 1 \right) \right], \quad (5)$$

where $s_\ell(s'_\ell)$ is the left neighbor of $s(s')$ and $s_r(s'_r)$ is the right neighbor of $s(s')$. $T_{s,s'}$ takes a value among $-2I$, $-I$, 0, I, and $2I$ depending on the liquid configuration around s and s' [see Fig. 1(d) for an example]. This specific implementation is motivated by the discrete models of growing surface displaying various self-affine structures [1,2].

The driving force is the sum of the pressure difference [Eq. (2)] and the effective tension [Eq. (5)]:

$$P_{s,s'} = \Delta p_{s,s'} + T_{s,s'}. \quad (6)$$

If $P_{s,s'} > 0$, the liquid can fill pore s with probability $\min\{P_{s,s'}, 1\}$ or just stays with probability $1 - \min\{P_{s,s'}, 1\}$. In case $P_{s,s'} < 0$, the liquid is retracted from s' with probability $\min\{|P_{s,s'}|, 1\}$ or stays with probability $1 - \min\{|P_{s,s'}|, 1\}$.

III. DISORDER-INDUCED STRONG ROUGHENING OF THE IMBIBITION FRONT

In this section, we study the impact of the disorder in the pore radii on the scaling behavior of the mean height and the roughness. We perform simulations of the lattice imbibition model for different lateral system sizes N, pore radii disorder strengths Δ, lateral correlation ranges of pressure R, and effective tension strengths I. The mean height H and the interface width (roughness) W are defined as

$$H = \langle \overline{y} \rangle = \left\langle \frac{1}{n(\mathcal{I})} \sum_{s \in \mathcal{I}} y_s \right\rangle,$$

$$W = \sqrt{\langle \overline{y^2} - \overline{y}^2 \rangle} \quad (7)$$

$$= \sqrt{\left\langle \frac{1}{n(\mathcal{I})} \sum_{s \in \mathcal{I}} y_s^2 - \left(\frac{1}{n(\mathcal{I})} \sum_{s \in \mathcal{I}} y_s \right)^2 \right\rangle},$$

where y_s is the y coordinate of the bottom end of a pore s, $\mathcal{I}$ is the interface, and $n(\mathcal{I})$ is the number of the pores belonging to the interface. $\overline{\cdots}$ indicates the average over the interface pores and $\langle \ldots \rangle$ indicates the average over different realizations of simulation. We typically average over 1000 realizations.

Given that $p_{(x,0)} = 0$ and $p^{(L)} \sim -1$, the pressure gradient $\Delta p_{s,s'}$ scales as $1/H$. Without the effective tension, one finds that

$$\frac{dH}{dt} \sim \overline{\Delta p_{s,s'}} \sim \frac{1}{H}, \quad (8)$$

which leads to the Lucas-Washburn's law $H \sim \sqrt{t}$. In our simulations, we observe the same behavior of height and pressure as above. We set $R = N/2$, i.e., the lateral correlation range of pressure equals the system size, as the sum in Eq. (4) runs over all possible x' values. We assume $I = 0$, i.e., there is no effective tension. Simulation results for average height
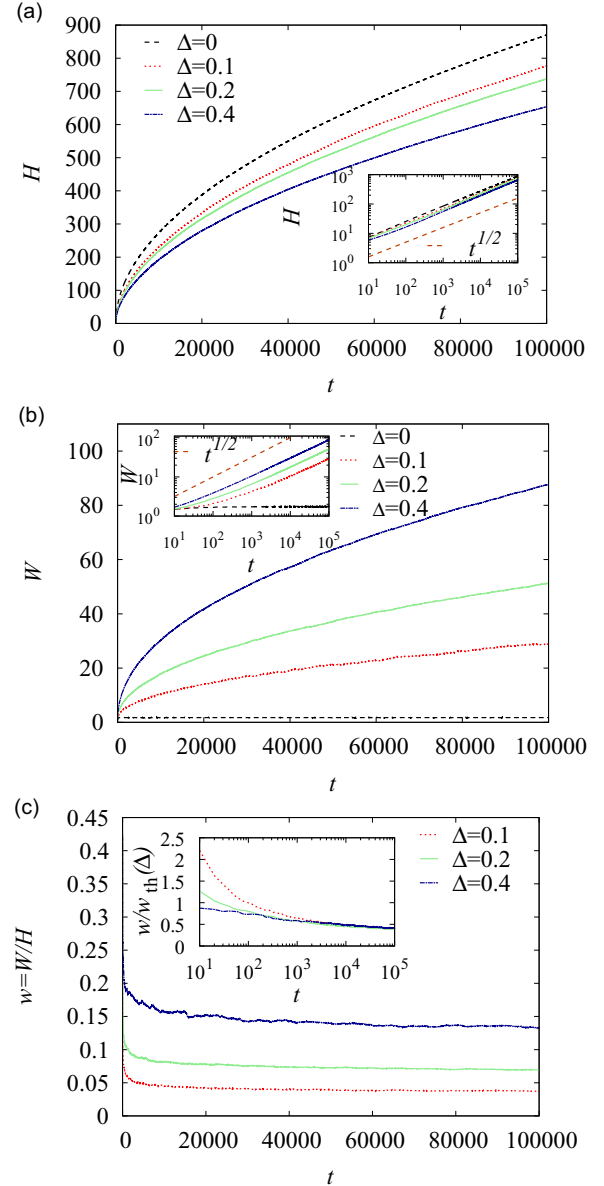

FIG. 3. (Color online) Time evolution of the mean height H and the roughness W for $N = 32$, $R = N/2$, $I = 0$, and different values of Δ. (a) Plots of H versus time t. Inset: The same plots in logarithmic scales showing that $H \sim t^{1/2}$. The bottom dashed line has slope $\frac{1}{2}$. (b) Plots of W versus t. Inset: The same plots in logarithmic scales showing that $W \sim t^{1/2}$. The smaller Δ is, the later the regime showing the square-root scaling appears. The top dashed line has slope $\frac{1}{2}$. (c) Plots of the relative roughness $w = \frac{W}{H}$ versus t. Inset: The ratio $\frac{w}{w_{\text{th}}(\Delta)}$ becomes independent of Δ in the long-time limit as predicted in Eq. (13).

and roughness are plotted in Figs. 3(a) and 3(b), respectively. We find that

$$H \sim t^B, \quad B = 0.53(5) \quad (9)$$

and

$$W \sim t^\beta, \quad \beta = 0.46(8). \quad (10)$$

The values of the scaling exponents B and β are both close to $\frac{1}{2}$, in agreement with the results obtained for the
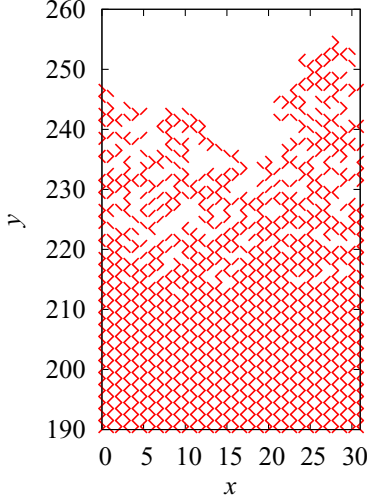
FIG. 4. (Color online) Liquid configuration at time $t = 10^4$ in the lattice imbibition model for $N = 32, \Delta = 0.1, R = N/2$, and $I = 0$.

pore-network model in Ref. [11]. The roughness W and the ratio W/H increase with disorder strength Δ, while the average height H decreases in accordance with [11]. For an ordered lattice, i.e., $\Delta = 0$, the roughness remains at a small value, meaning that the interface is smooth, while the mean height increases. A typical liquid configuration for a disordered lattice is shown in Fig. 4. One observes a large number voids generated by thick pores with a Laplace pressure $p^{(L)}$ that is larger than the hydrostatic pressure at the junction, preventing the filling of the pore [24]. For any nonvanishing disorder strength $\Delta > 0$, the interface is rough and the ratio W/H is nonzero.

Along the boundaries of voids the Laplace pressure $p^{(L)}$ is larger than the hydrostatic pressure within the nearest pore junction. Since the hydrostatic pressure $p_{(x,y)}$ decreases with increasing y, the voids are more likely to emerge as the height y increases. The lowest possible height y_{min} for which voids may exist can be obtained by equating the hydrostatic pressure and the largest possible value of the Laplace pressure $p^{(L)}_{(max)}$. The hydrostatic pressure at y is estimated as $\langle p \rangle(y) \simeq \langle p^{(L)} \rangle \frac{y}{H}$ with H the mean height. Therefore, at $y = y_{min}$, it holds that

$$\langle p^{(L)} \rangle \frac{y_{min}}{H} = p^{(L)}_{max}. \qquad (11)$$

The pore radii are distributed uniformly between $1 - \Delta$ and $1 + \Delta$, and therefore $\langle p^{(L)} \rangle = -\langle \frac{1}{r} \rangle = -\frac{1}{2\Delta} \ln \frac{1+\Delta}{1-\Delta}$ and $p^{(L)}_{max} = -\frac{1}{1+\Delta}$. Using these relations in Eq. (11), we find that $\frac{H}{y_{min}} = \frac{1+\Delta}{2\Delta} \ln(\frac{1+\Delta}{1-\Delta})$. $H - y_{min}$ is an estimate for the front width and the relative width w_{th} obeys

$$w_{th} \simeq \frac{H - y_{min}}{H} = 1 - \frac{2\Delta}{1+\Delta} \left[\ln \left(\frac{1+\Delta}{1-\Delta} \right) \right]^{-1}. \qquad (12)$$

We conjecture that the relative roughness $w = W/H$ scales in the same way as w_{th}:

$$w \simeq w_{th} \simeq \Delta \quad \text{for} \quad \Delta \ll 1, \qquad (13)$$

which is consistent with the simulation results in Figs. 3(b) and 3(c), where $W/H \simeq 0$ for $\Delta = 0$ and W/H increases with Δ. In addition, the long-time limit of w/w_{th} becomes

independent of Δ as shown in the inset of Fig. 3(c) in agreement with Eq. (13). From the simulation results and the analytical argument we conclude that the disorder in the pore radii is crucial for the interface roughening of imbibition in the elongated-pore systems.

IV. IMPACT OF THE PRESSURE CORRELATION

In this section, we explore the impact of the correlation range of pressure R on the roughness of imbibition front. If $R = 1$, only the zeroth-order pressures $p^{(0)}$ of the two pores touching the junction point (x, y) are used to evaluate $p_{(x,y)}$ according to Eq. (4). $p_{(x,y)}$ may fluctuate not only with y, but also with x as if the vertical columns were separated. On the contrary, if $R \geqslant N/2$, $p_{(x,y)}$ is the average of $p^{(0)}_{(x',y)}$'s for all x', which does not vary with x for given y. It seems plausible to assume that the liquid-volume conservation in the elongated-pore systems makes the lateral correlation of pressure long ranged, i.e., $R \geqslant N/2$ in our model.

For $R = 1$, one expects a roughening exponent $\beta = \frac{1}{4}$: In this case, the height in each column evolves with time independently from the neighbor and one can expect random deposition behavior, in which case the height-height fluctuations between the columns evolve as $W \sim \sqrt{\langle h \rangle} \sim t^{1/4}$, which can also be seen as follows. The interface height h in a single column evolves with time as $\frac{dh}{dt} = \frac{1}{\xi(h)h}$, where $\langle \xi \rangle = c$ and $\langle \xi(h)\xi(h') \rangle - \langle \xi \rangle^2 = d\delta(h - h')$ with c and d some constants [11]. The time taken for the interface to reach h satisfies statistically $\langle t \rangle \sim h^2$ and $\langle t^2 \rangle - \langle t \rangle^2 \sim h^{3/2}$, which yields equivalently $\langle h \rangle \sim t^{1/2}$ and $W \sim \sqrt{\langle h^2 \rangle - \langle h \rangle^2} \sim t^{1/4}$ [11].

Our lattice imbibition model demonstrates that the mean height $H(t)$ is not affected by the correlation range R. On the other hand, the roughness is strongly affected by R. The scaling exponent β introduced in Eq. (10) turns out to be very close to $\frac{1}{4}$ for $R = 1$ and increases to $\frac{1}{2}$ with increasing R as shown in Fig. 5. The data shown in Fig. 5 indicate that in the infinite system size limit $N \to \infty$ the universality class of the roughening process changes from the random deposition
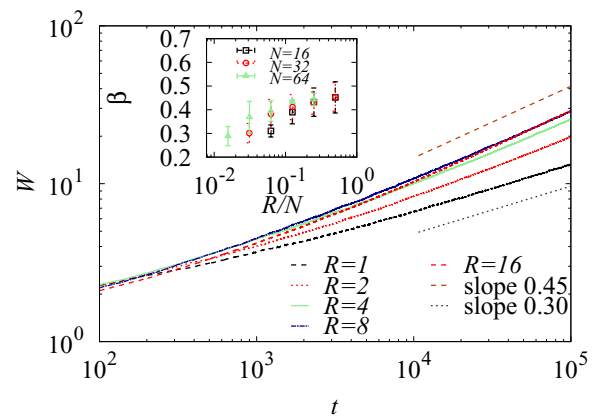

FIG. 5. (Color online) Roughness W as a function of time t for $N = 32$, $I = 0$, $\Delta = 0.1$, and different ranges R of pressure correlation. The roughness increases with time as $W \sim t^\beta$ with β increasing with R. The top dashed line and the bottom dotted line have slopes 0.45 and 0.3, respectively. Inset: The exponent β as a function of R/N for different N's.
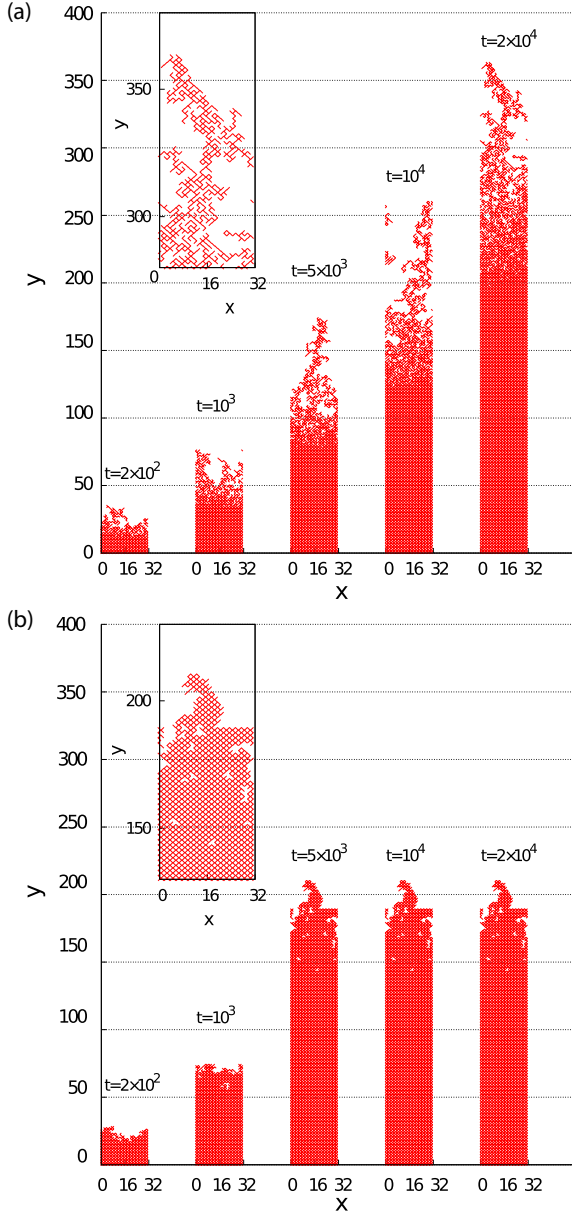
FIG. 6. (Color online) Time evolution of the liquid configuration with (a) $I = 0$ and (b) $I = 0.08$ for $N = 32$, $\Delta = 0.4$, $R = N/2$. The insets show magnified views at $t = 2 \times 10^4$ (a) for $280 \leqslant y \leqslant 380$ and (b) for $130 \leqslant y \leqslant 230$. The effective tension makes the cluster of filled pores more compact than without tension and leads the front to stop in the long-time limit.

universality class ($\beta = \frac{1}{4}$) for finite R (i.e., $R/N \to 0$) to the spontaneous imbibition universality class ($\beta = \frac{1}{2}$) for infinite R (i.e., $R \propto N$).

V. IMPACT OF THE EFFECTIVE TENSION

The driving force $P_{s,s'}$ consists of the effective tension $T_{s,s'}$ as well as the pressure difference $\Delta p_{s,s'}$. $T_{s,s'}$ in Eq. (5) ranges between $-2I$ and $2I$, thus, it may contribute to both filling an empty pore s or emptying a filled pore s'. While the effective tension remains of order I, the pressure difference decreases with time as $\Delta p_{s,s'} \sim H^{-1}$. The evolution of the
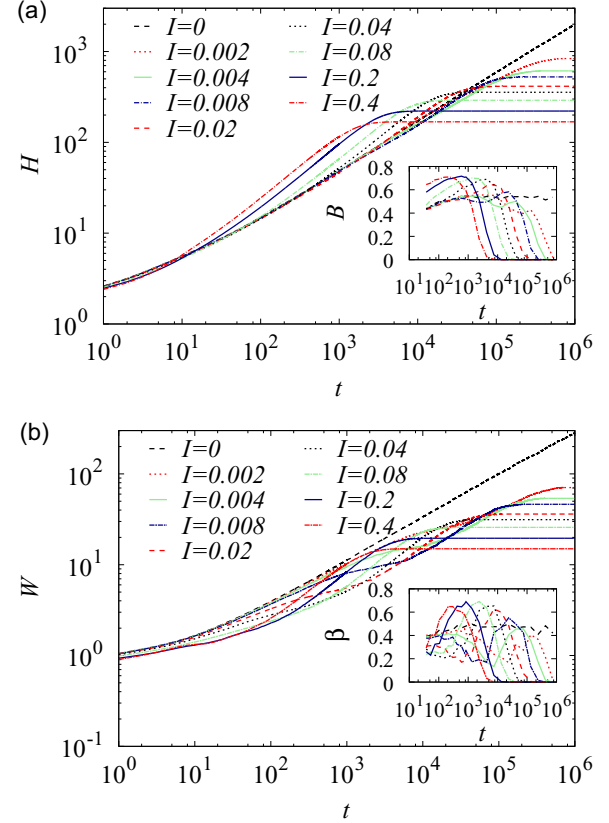

FIG. 7. (Color online) Time evolution of the mean height H and the roughness W under the effective tension for $N = 64$, $R = N/2$, $\Delta = 0.4$, and different values of I. (a) Plots of H versus time t. H grows faster with $I > 0$ than with $I = 0$ in the intermediate-time regime and saturates in the long-time limit. Inset: The estimated exponent B in the relation $H \sim t^B$ increases from 0.5 to 0.7 before the saturation of H. (b) Plots of W versus t. The roughness is not larger with $I > 0$ than that with $I = 0$ in the whole time regime. As the mean height does, the roughness increases faster with $I > 0$ than with $I = 0$ in the intermediate-time regime and saturates in the long-time limit. Compared with the mean height, the time-dependent behavior of W is complicated. Inset: The estimated exponent β in the relation $W \sim t^\beta$ finds its maximum value around 0.7.

liquid configurations with and without the effective tension at different times is presented in Fig. 6. The time evolution of the mean height H and the roughness W are shown in Fig. 7 for different strengths of the effective tension I. The most important impact of tension is that the imbibition front propagation stops at some point and its roughness saturates. Moreover, the tension smoothes the interface. The roughness is smaller with tension ($I > 0$) than without it ($I = 0$). The clusters of filled pores in presence of tension are more compact than those without tension (see Fig. 6). For $I \ll 1$, in the early-time regime, the pressure differences are larger than the effective tension and the dynamical evolution of height and roughness is similar to the case without tension ($I = 0$). For longer times, the pressure differences decrease and become comparable to the effective tension. In the intermediate-time regime, H and W grow faster with tension than without. The liquid propagation eventually stops because the pressure differences drop below the effective tension. The larger I,

the earlier the long-time regime begins and the smaller the saturation values of H and W. These observations also depend on the system size N.

To understand the impact of the effective tension on the roughening of the imbibition front, we explore quantitatively the behavior of H and W on I and N. We take the scaling ansatz for the behavior of H and W and estimate the associated scaling exponents by their data collapse around the boundaries of the distinct time regimes, which allows us to see the width of each time regime. As the mean height and the roughness behave in different ways, we study them separately.

A. Scaling behavior of the mean height H

As shown in Fig. 7(a), three regimes appear in the time evolution of H with characteristic time scales t_1 and t_H. In the short-time regime $t \ll t_1$, $H \sim t^B$ with the same exponent as in Eq. (9) regardless of I. In the intermediate-time regime $t_1 \ll t \ll t_H$, the mean height grows faster than the former case, i.e., $H \sim t^{B_*}$ with $B_* > B$. In the long-time limit $t \gg t_H$, the liquid does not propagate anymore and the height saturates to H_{sat}. In summary,

$$H \sim \begin{cases} t^B & \text{for} \quad t \ll t_1, \\ t^{B_*} & \text{for} \quad t_1 \ll t \ll t_H, \\ H_{\text{sat}} & \text{for} \quad t \gg t_H. \end{cases} \quad (14)$$

The effective scaling exponent $B(t)$, given in the inset of Fig. 7(a), can be estimated as $B(t) = \ln[\frac{H(t+\delta t)}{H(t)}]/\ln[\frac{t+\delta t}{t}]$ for a time window δt around time t. By averaging $B(t)$ around its maximum, we estimate B_* as[1]

$$B_* = 0.70(5) \quad (15)$$

for $\Delta = 0.4$, which is not significantly different from $B_* = 0.73(10)$ for $\Delta = 0.1$.

We find that around the first crossover time t_1, the simulation data for different values of I and N collapse onto a single curve showing the crossover behavior under the following scaling form:

$$H = t_1^B \Phi_1\left(\frac{t}{t_1}\right), \quad \text{where}$$

$$t_1 = I^{-\eta_1} \quad \text{and} \quad (16)$$

$$\Phi_1(x) \sim \begin{cases} x^B & \text{for} \quad x \ll 1, \\ x^{B_*} & \text{for} \quad x \gg 1. \end{cases}$$

The corresponding scaled data are shown in Fig. 8. The exponent η_1 equals 2.0(1).

After the fast growth in the intermediate regime ($H \sim t^{B_*}$), H eventually saturates to its maximum value over the crossover time t_H. The saturation values shown in Fig. 9 scale with the system size N and the effective tension I as

$$H_{\text{sat}} \sim I^{-\nu_H} N^{\alpha_H}. \quad (17)$$

The values of exponents ν_H and α_H are given in Table I for $\Delta = 0.1$ and 0.4.

_____

[1] B is estimated by the average value of $B(t)$ in the very early-time regime and B_* by the average value of $B(t)$ around the time when $B(t)$ is maximum. These average values still vary with I and N, and these variations are included in their error bars.
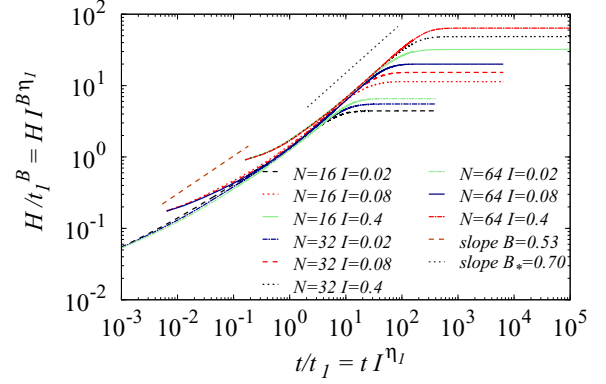

FIG. 8. (Color online) Collapse of the scaled data $H/t_1^B = HI^{B\eta_1}$ as functions of $t/t_1 = tI^{\eta_1}$ with $\eta_1 = 2.0$ and $B = 0.53$ for $\Delta = 0.4$ and different values of system size N and the effective tension I [see Eq. (16)]. Two lines with slopes $B = 0.53$ and $B_* = 0.70$, respectively, as in Eqs. (9) and (15) are also drawn.

Using Eq. (17), one finds the following scaling functions for $H(t)$ in the case of finite t/t_H:

$$H = I^{-\nu_H} N^{\alpha_H} \Phi_H\left(\frac{t}{t_H}\right), \quad \text{where}$$

$$t_H = I^{-\eta_H} N^{z_H} \quad \text{and}$$

$$\Phi_H(x) \sim \begin{cases} x^{B_*} & \text{for} \quad x \ll 1, \\ 1 & \text{for} \quad x \gg 1, \end{cases} \quad \text{with} \quad (18)$$

$$\eta_H = \frac{\eta_1(B_* - B) + \nu_H}{B_*} \quad \text{and}$$
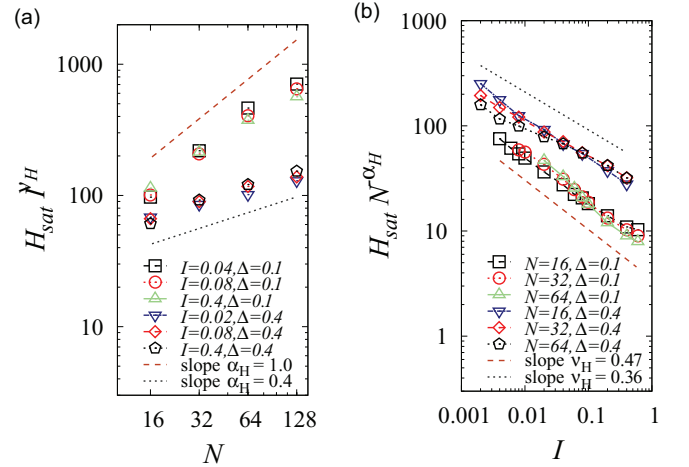
$$z_H = \frac{\alpha_H}{B_*}.$$

FIG. 9. (Color online) Scaling behavior of the saturation height H_{sat} with respect to the system size N and the effective tension strength I. (a) Collapse of the plots of $H_{\text{sat}} I^{\nu_H}$ versus N for different I's and given Δ. The upper collapsed data are for $\Delta = 0.1$ and the lower for $\Delta = 0.4$. (b) Collapse of $H_{\text{sat}} N^{-\alpha_H}$ versus I for different N's and given Δ. The upper collapsed data are for $\Delta = 0.4$ and the lower for $\Delta = 0.1$. The data collapse in both plots are found with $\nu_H = 0.47$ and $\alpha_H = 1.0$ for $\Delta = 0.1$ and $\nu_H = 0.36$ and $\alpha_H = 0.4$ for $\Delta = 0.4$.

TABLE I. The scaling exponents for the mean height H and the roughness W. See the main text for their definitions.

	H			W	
	$\Delta = 0.1$	$\Delta = 0.4$		$\Delta = 0.1$	$\Delta = 0.4$
B	0.53(5)	0.53(3)	β	0.46(5)	0.46(6)
B_*	0.73(10)	0.70(5)	β_*	0.76(10)	0.67(5)
η_1	2.0(1)	2.0(1)	η_2	1.2(1)	1.2(1)
α_H	1.0(1)	0.4(1)	α_W	1.1(1)	0.5(1)
ν_H	0.47(10)	0.36(4)	ν_W	0.45(9)	0.33(8)
η_H	1.2	1.0	η_W	1.3	1.1
z_H	1.4	0.6	z_W	1.1	0.45
			θ	0.40(5)	0.43(5)
			ζ	0.3(1)	0.2(1)

The data collapse is shown in Fig. 10. All exponents obtained from the simulation are presented in Table I.

Equations (16) and (18) indicate that the fast growth $H \sim t^{B_*}$ with $B_* \sim 0.7$ appears in a wide range of times when I has a nonzero finite value and N is large: the intermediate regime begins at $t_1 = I^{-\eta_1} = \mathcal{O}(1)$ and ends at $t_H = I^{-\eta_H} N^{z_H} \gg 1$ for $N \gg 1$. The intermediate regime is observed as long as $t_H \gg t_1$ or, equivalently,

$$I \gg N^{-\frac{z_H}{\eta_1 - \eta_H}}. \tag{19}$$

If the effective tension is so small as to violate Eq. (19), the square-root growth of the mean height would persist until saturation occurs.

B. Scaling behavior of the roughness W

The behavior of the roughness is more complicated than the mean height as seen in Fig. 7(b). Here, four regimes are observed which display distinct behavior of W as

$$W \sim \begin{cases} t^\beta & \text{for} \quad t \ll t_0, \\ \text{slowly increasing} & \text{for} \quad t_0 \ll t \ll t_2, \\ t^{\beta_*} & \text{for} \quad t_2 \ll t \ll t_W, \\ W_{\text{sat}} & \text{for} \quad t \gg t_W. \end{cases} \tag{20}$$

Among these regimes, the first two are rather difficult to identify. We expect $W \sim t^\beta$ in the first regime, $t \ll t_0$, but its duration is rather short. For the same reason, the behavior of W is not clearly seen in the second regime. To make these early-time regimes long enough, the model with much smaller values of I for much longer time should be simulated than in this study. We restrict ourselves to the scaling behavior of W around $t = t_2$ and $t = t_W$. In the third regime, $t_2 \ll t \ll t_W$, fast growth $W \sim t^{\beta_*}$ with $\beta_* > \beta \sim 0.5$ is observed, which eventually saturates over $t \gg t_W$.

We estimate the effective scaling exponent $\beta(t)$ [inset of Fig. 7(b)] in a similar way we argued for height. While we observe a nearly constant value $\beta(t) \simeq 0.46$ for $I = 0$ for the whole time period, $\beta(t)$ varies with time when $I > 0$. We find $\beta_* = 0.67(5)$ for $\Delta = 0.4$ and $\beta_* = 0.76(10)$ for $\Delta = 0.1$.

Around $t = t_2$, the curvature of $W(t)$ changes and $W(t)$ grows as t^{β_*} for $t \gg t_2$. Assuming that the value of $W(t_2)$ scales with the tension I and the system size N as $W(t_2) \sim I^{-\theta} N^\zeta$, where θ and ζ are new scaling exponents, we find that the scaled data of the roughness for different N's and I's collapse onto a curve in the regime $t \gg t_2$ as

$$W = I^{-\theta} N^\zeta \, \Phi_2\left(\frac{t}{t_2}\right), \quad \text{where}$$

$$t_2 = I^{-\eta_2}, \quad \text{and} \tag{21}$$

$$\Phi_2(x) \sim x^{\beta_*} \quad \text{for} \quad x \gg 1$$

as presented in Fig. 11. Here, the scaling exponents are $\theta \simeq 0.43$, $\zeta \simeq 0.2$, and $\eta_2 \simeq 1.2$ for $\Delta = 0.4$. In these exponents, there is no significant difference between $\Delta = 0.1$ and 0.4 (see Table I).

The saturation value of the roughness W_{sat} for $t \gg t_W$ scales as

$$W_{\text{sat}} \sim I^{-\nu_W} N^{\alpha_W} \tag{22}$$

with the exponents given by $\nu_W = 0.33(8)$ and $\alpha_W = 0.5(1)$ for $\Delta = 0.4$ as shown in Fig. 12. Around t_W, the following
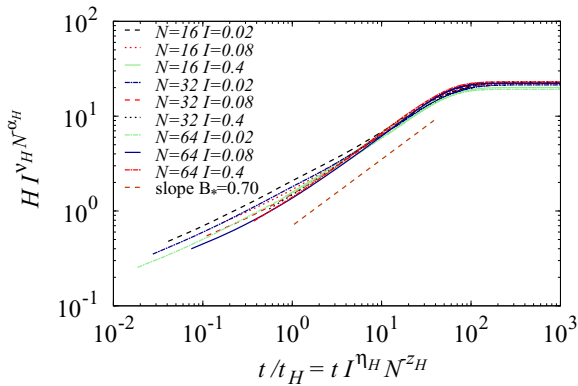

FIG. 10. (Color online) Collapse of the scaled data $H I^{\nu_H} N^{-\alpha_H}$ as functions of the scaling variable $t/t_H = t I^{\eta_H} N^{-z_H}$ for $\Delta = 0.4$ and different values of N and I [see Eq. (18)]. The values of the scaling exponents are $\nu_H = 0.36$, $\alpha_H = 0.4$, $\eta_H = 1.0$, and $z_H = 0.6$. The bottom dashed line has slope $B_* = 0.70$.
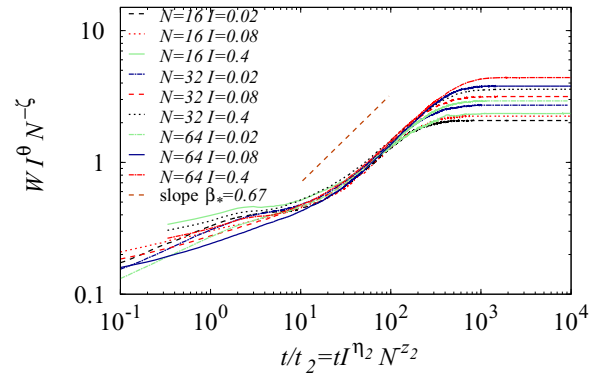

FIG. 11. (Color online) Collapse of the scaled data of $W I^\theta N^{-\zeta}$ as functions of $t/t_2 = t I^{\eta_2}$ for $t/t_2 \gg 1$ with $\eta_2 = 1.2$, $\theta = 0.43$, and $\zeta = 0.2$ for $\Delta = 0.4$ and different values of system size N and the effective tension I [see Eq. (21)]. The top dashed line has slope $\beta_* = 0.67$ as in Eq. (10).
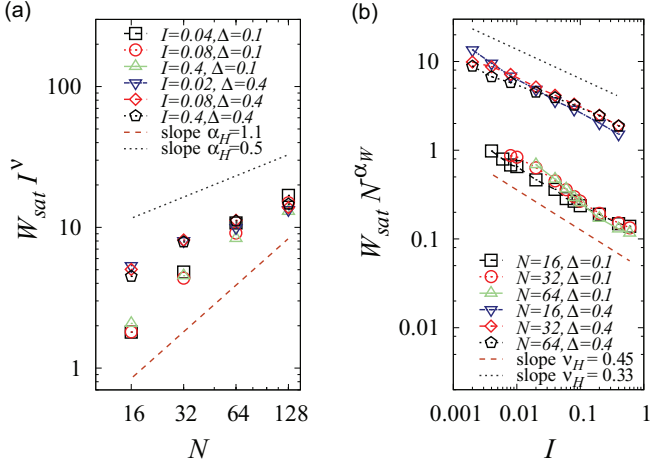
FIG. 12. (Color online) Scaling behavior of the saturation roughness W_{sat} with respect to the system size N and the effective tension strength I. (a) Collapse of the plots of $W_{sat} I^{\nu_W}$ versus N for different I's and given Δ. The upper collapsed data are for $\Delta = 0.4$ and the lower for $\Delta = 0.1$. (b) Collapse of $W_{sat} N^{-\alpha_W}$ versus I for different N's and given Δ. The upper collapsed data are for $\Delta = 0.4$ and the lower for $\Delta = 0.1$. The data collapse in both plots are found with $\nu_W = 0.45$ and $\alpha_W = 1.1$ for $\Delta = 0.1$ and $\nu_W = 0.33$ and $\alpha_W = 0.5$ for $\Delta = 0.4$.

scaling function $\Phi_W(x)$ characterizes the behavior of W:

$$W = I^{-\nu_W} N^{\alpha_W} \Phi_W\left(\frac{t}{t_W}\right), \quad \text{where}$$

$$t_W = I^{-\eta_W} N^{z_W} \quad \text{and}$$

$$\Phi_W(x) \sim \begin{cases} x^{\beta_*} & \text{for} \quad x \ll 1, \\ 1 & \text{for} \quad x \gg 1 \end{cases} \quad \text{with} \quad (23)$$

$$\eta_W = \eta_2 - \frac{\theta - \nu_W}{\beta_*} \quad \text{and}$$

$$z_W = \frac{\alpha_W - \zeta}{\beta_*}.$$

The resulting scaled data are presented in Fig. 13 and the exponents are given in Table I.

The mean height and the roughness have quite similar scaling properties in the intermediate- and long-time regimes; both H and W grow as a power law with $B_*, \beta_* \simeq 0.7$ which is larger than 0.5 obtained in absence of effective tension I, and saturate at the values which scale as $I^{-\nu} N^{\alpha}$ with $\nu \simeq 1$ and $0.4 \lesssim \alpha \lesssim 1.4$ and thus diverge in the limits $N \to \infty$ and $I \to 0$.

C. Understanding the scaling behavior in the intermediate and long times

The scaling of interface height and roughness in the intermediate-time regime, their saturation in the long-time regime, as well as the values of the exponents B_* and β_* ($\simeq 0.7$) are reminiscent of what is observed during the motion of interfaces in random environments close to the depinning transition point [20]. The dynamics and roughening of the interface vary with the density of pinning centers and are governed by the mechanism of directed percolation (DP) in the
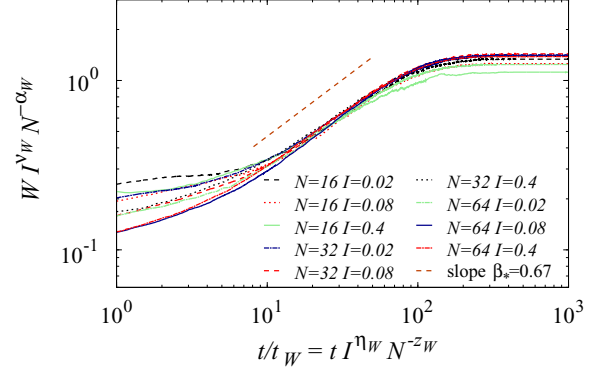

FIG. 13. (Color online) Collapse of the scaled data $W I^{\nu_W} N^{-\alpha_W}$ as functions of the scaling variable $t/t_W = t I^{\eta_W} N^{-z_W}$ for $\Delta = 0.4$ and different values of N and I [see Eq. (23)]. The scaling exponents are $\nu_W = 0.33$, $\alpha_W = 0.5$, $\eta_W = 1.1$, and $z_W = 0.45$. The top dashed line has slope $\beta_* = 0.67$.

vicinity of the pinning-depinning transition point. The pinned nodes form a cluster which is qualitatively equivalent to the DP cluster, and the scaling behavior of the latter determines various properties of the interface. In the imbibition model studied in this work, the driving force is provided by the Laplace pressure, which depends on the pore radii and is thus a random force. Pinning appears when the hydrostatic pressure is much lower than the Laplace pressure of the meniscus which is relevant in thick pores, and when the effective tension forbids the liquid from propagating or even retracts the liquid that has proceeded.

Let us compare our results to the scaling properties of the DP clusters. Suppose the pinning cluster, the cluster of pores suppressing the liquid propagation, is as large as $\xi_\perp$ in the perpendicular (y) direction and as $\xi_\parallel$ in the lateral (x) direction. If this cluster is a DP cluster, those length scales scale as

$$\xi_\perp \sim |q - q_c|^{-\nu_\perp}, \quad \xi_\parallel \sim |q - q_c|^{-\nu_\parallel} \quad (24)$$

with q being the density of pinning center and q_c the critical point. The mean height and the roughness are set commonly by $\xi_\perp$ and the time scale is set by $\xi_\parallel$ as $H \sim W \sim \xi_\perp \Phi(t/\xi_\parallel)$ [20]. If the pinning density is so close to the critical point that ξ is larger than the lateral system size N, the lateral size of the cluster is set by N and

$$H \sim N^{\nu_\perp/\nu_\parallel} \Phi\left(\frac{t}{N}\right), \quad W \sim N^{\nu_\perp/\nu_\parallel} \Psi\left(\frac{t}{N}\right), \quad (25)$$

where the scaling function behaves as

$$\Phi(x) \sim \Psi(x) \sim \begin{cases} x^{\nu_\perp/\nu_\parallel} & \text{for} \quad x \ll 1, \\ \text{const} & \text{for} \quad x \gg 1. \end{cases} \quad (26)$$

Note that the scaling exponent $\nu_\perp/\nu_\parallel \simeq 0.633$ and the dynamic exponent z is 1 in this argument [26].

The scaling behavior of H and W in the lattice imbibition model with tension ($I > 0$) is similar to Eqs. (25) and (26) in the intermediate regime: Both the scaling exponent B_* and β_* are close to the value of $\nu_\perp/\nu_\parallel \simeq 0.633$, which indicates that our imbibition model with tension might be in the same universality class as the DP clusters. However, in contrast to interface growth in a disordered environment (DPD), the

pinning in our model is not static but dynamically generated and the driving force decreases with time as the pressure gradient decreases. Moreover, the dynamic exponents z_H and z_W deviate from 1 for the case of strong disorder ($\Delta = 0.4$) of the pore radii considered in this work.

VI. CONCLUSION AND DISCUSSION

In this work, we introduced a lattice model for spontaneous imbibition, which follows the same design principles as other interface growth models on a lattice. The emergent similarities facilitate a comparison of the characteristics of imbibition front propagation with other growth models in random environments and help to identify a minimal set of physical mechanisms that could explain the experimental observations [11]. In particular, we have shown quantitatively how the disorder in the pore thickness and the lateral correlation of hydrostatic pressure caused by liquid-volume conservation affect the roughening of the imbibition front in the elongated-pore systems. Also, we found that the presence of an effective tension changes the scaling properties of the front and leads to multiple crossovers in the dynamical evolution of height and roughness. The effective tension suppresses the formation of voids and smoothes the clusters of filled pores. As a result, with tension the imbibition front propagates faster and the roughness increases faster in the intermediate-time regime than that without the effective tension. Ultimately, the imbibition front stops to propagate. By extensive simulations, we have identified the scaling behavior depending on the strength of the tension and the system size.

Despite the approximation adopted in computing the hydrostatic pressure, the simulation is still time consuming, which restricted the study to small system sizes. As a result, it is hard to increase the accuracy of the estimated scaling exponents. While some scaling exponents in this study are close to those of the directed percolation class, there are

differences as well: the pinning centers are not quenched but dynamically generated and the dynamic exponent is found to deviate from that of the DP class for strong disorder in the pore radii, suggesting a new universality class. Thus, it remains an open question as to whether the proposed lattice imbibition model belongs to the directed percolation universality class or represents a novel one.

While we introduced the correlation range and the effective surface tension strength as free parameters, a rigorous derivation and their comparison with real systems would be desirable. Since our model predicts that an effective tension changes the asymptotic behavior of the front propagation drastically, it would be interesting to study experimentally the spontaneous imbibition of nanoporous materials in which one could change the aspect ratio of pores (i.e., the typical ratio between pore radius and pore length): The Vycor glass studied in Ref. [11] contained a network of elongated pores (aspect ratio around 5) and one would expect an effective tension to be absent since menisci in different pores are well separated. For aspect ratios around 1, the size of the menisci becomes comparable to the length of the pores (depending on wetting angle) and the menisci at junctions start to coalesce leading to a connected liquid-air interface. We propose that our imbibition model captures this situation by a nonvanishing effective tension, and predict that in this case neither the Lucas-Washburn law nor the roughening exponent $\beta = \frac{1}{2}$ continues to hold. With nanoporous materials one should even be able to reach the predicted asymptotic late-time regime, for which our model predicts the imbibition front propagation to cease.

[1] A.-L. Barabási and H. Stanley, *Fractal Concepts in Surface Growth* (Cambridge University Press, Cambridge, UK, 1995).

[2] P. Meakin, *Fractals, Scaling and Growth Far From Equilibrium* (Cambridge University Press, Cambridge, UK, 1998).

[3] M. Kardar, G. Parisi, and Y. C. Zhang, Phys. Rev. Lett. **56**, 889 (1986).

[4] M. Alava, M. Dubé, and M. Rost, Adv. Phys. **53**, 83 (2007).

[5] M. A. Rubio, C. A. Edwards, A. Dougherty, and J. P. Gollub, Phys. Rev. Lett. **63**, 1685 (1989).

[6] R. Lenormand, J. Phys.: Condens. Matter **2**, SA79 (1990).

[7] R. Lenormand, E. Touboul, and C. Zarcone, J. Fluid Mech. **189**, 165 (1988).

[8] M. J. Blunt and H. Scher, Phys. Rev. E **52**, 6387 (1995).

[9] E. Aker, K. J. Måløy, and A. Hansen, Phys. Rev. E **58**, 2217 (1998).

[10] C.-H. Lam and V. K. Horváth, Phys. Rev. Lett. **85**, 1238 (2000).

[11] S. Gruener, Z. Sadjadi, H. E. Hermes, A. V. Kityk, K. Knorr, S. U. Egelhaaf, H. Rieger, and P. Huber, Proc. Natl. Acad. Sci. USA **109**, 10245 (2012).

[12] J. Krug and P. Meakin, Phys. Rev. Lett. **66**, 703 (1991).

[13] V. Ganesan and H. Brenner, Phys. Rev. Lett. **81**, 578 (1998).

[14] M. Dubé, M. Rost, K. R. Elder, M. Alava, S. Majaniemi, and T. Ala-Nissila, Phys. Rev. Lett. **83**, 1628 (1999).

[15] P. Kechagia, Y. C. Yortsos, and P. Lichtner, Phys. Rev. E **64**, 016315 (2001).

[16] L. Paterson, Phys. Rev. Lett. **52**, 1621 (1984).

[17] R. Lenormand and C. Zarcone, Phys. Rev. Lett. **54**, 2226 (1985).

[18] R. Lucas, Kolloid Z. **23**, 15 (1918).

[19] E. W. Washburn, Phys. Rev. **17**, 273 (1921).

[20] L.-H. Tang and H. Leschhorn, Phys. Rev. A **45**, R8309 (1992).

[21] S. V. Buldyrev, A.-L. Barabási, F. Caserta, S. Havlin, H. E. Stanley, and T. Vicsek, Phys. Rev. A **45**, R8313 (1992).

[22] H. Leschhorn, Phys. Rev. E **54**, 1313 (1996).

[23] D. Geromichalos, F. Mugele, and S. Herminghaus, Phys. Rev. Lett. **89**, 104503 (2002).

[24] Z. Sadjadi and H. Rieger, Phys. Rev. Lett. **110**, 144502 (2013).

[25] R. Lenormand, C. Zarcone, and A. Sarr, J. Fluid Mech. **135**, 337 (1983).

[26] L. A. N. Amaral, A.-L. Barabási, S. V. Buldyrev, S. T. Harrington, S. Havlin, R. Sadr-Lahijany, and H. E. Stanley, Phys. Rev. E **51**, 4655 (1995).